Loss cone-driven cyclotron maser instability

Sang-Yun Lee,[1] Sibaek Yi,[1] Dayeh Lim,[1] Hee-Eun Kim,[1]
Jungjoon Seough,[1] and Peter H. Yoon[1,2]

Received 12 August 2013; revised 9 October 2013; accepted 27 October 2013.

[1] The weakly (or mildly) relativistic cyclotron maser instability has been successfully applied to explain the Earth's auroral kilometric radiation and other radio sources in nature and laboratory. Among the most important physical parameters that determine the instability criteria is the ratio of plasma-to-electron cyclotron frequencies, ω_p/Ω. It is therefore instructive to consider how the normalized maximum growth rate, $\gamma_{\max}/\Omega$, varies as a function of ω_p/Ω. Although many authors have already discussed this problem, in order to complete the analysis, one must also understand how the radiation emission angle corresponding to the maximum growth, $\theta_{\max}$, scales with ω_p/Ω, since the propagation angle determines the radiation beaming pattern. Also, the behavior of the frequency corresponding to the maximum growth rate at each harmonic, $(\omega_{\max} - s\Omega)/\Omega$, where $s = 1, 2, 3, \ldots$, as a function of ω_p/Ω is of importance for a complete understanding of the maser excitation. The present paper computes these additional quantities for the first time, making use of a model loss cone electron distribution function.

Citation: Lee, Sang-Yun, Sibaek Yi, Dayeh Lim, Hee-Eun Kim, Jungjoon Seough, and Peter H. Yoon (2013), Loss cone-driven cyclotron maser instability, *J. Geophys. Res. Space Physics*, *118*, doi:10.1002/2013JA019298.

1. Introduction

[2] Within the space and astrophysical context, the weakly relativistic cyclotron maser instability received much attention in the 1980s and early 1990s when it was discovered in the 1970s that the Earth was a strong radio wave-emitting planet [e.g., see *Gurnett*, 1974; *Benson et al.*, 1980]. The essential physical explanation for the terrestrial (or auroral) kilometric radiation (AKR for short) was provided by *Wu and Lee* [1979] in terms of the maser instability mechanism. Since then, many researchers devoted their efforts on the theoretical investigation of the cyclotron maser instability [*Lee and Wu*, 1980; *Hewitt et al.*, 1982; *Melrose et al.*, 1984] as well as on numerical simulations thereof [*Pritchett*, 1984, 1985, 1986; *Winglee and Pritchett*, 1986; *Pritchett and Winglee*, 1989; *Pritchett et al.*, 1999; *Lee et al.*, 2009; *Speirs et al.*, 2010]. As a result of these efforts, many details associated with the cyclotron maser instability are well known (see, e.g., the recent review by *Treumann* [2006]).

[3] Applications of the cyclotron maser instability to other astrophysical sources beyond the Earth have also been made. For instance, *Zarka* [1998], *Gurnett et al.* [2004], *Hess et al.* [2007], and *Menietti et al.* [2010] applied the cyclotron maser mechanism to radio emissions from magnetized planets in our solar system. A survey of recent literature also shows that the cyclotron maser mechanism is being employed for other astrophysical bodies such as for the solar radio bursts [*Tang and Wu*, 2009; *Zhao et al.*, 2013], radio emissions from extrasolar planets [*Farrell et al.*, 1999], radiation at the astrophysical shock fronts [*Bingham et al.*, 2003], and radio emissions from various stellar environments [*Willes and Wu*, 2004; *Begelman et al.*, 2005; *Hallinan et al.*, 2007, 2008; *Trigilio et al.*, 2011; *Nichols et al.*, 2012].

[4] From a theoretical standpoint, even though the fundamentals of the cyclotron maser instability are well known, there still exist some unresolved and outstanding issues. One of them is the fine structure associated with AKR emission [*Gurnett et al.*, 1979]. Despite various theories proposed thus far [*Calvert*, 1982; *Melrose*, 1986a; *Yoon and Weatherwax*, 1998a; *Pritchett et al.*, 1999; *Pottelette et al.*, 2003; *Treumann et al.*, 2011], there is no consensus. Another issue has to do with the source mechanism for the cyclotron maser excitation. The early theory by *Wu and Lee* [1979] favored the loss cone and the associated positive perpendicular gradient in the electron velocity distribution function, but some later authors variably argued for the trapped electrons [*Louran et al.*, 1990], the shell or the horseshoe feature associated with the electrons reflected by the combined mirror force and parallel electrostatic field [*Bingham et al.*, 2004; *Ergun et al.*, 2000] as the source.

[5] Most theories of cyclotron maser instability are developed for homogeneous plasmas. There have been some efforts to extend the analysis to cavity-like or cylindrical geometry [*Pritchett*, 1986; *Pritchett and Winglee*, 1989; *Louarn and Le Qu'eau*, 1996; *Vorgul et al.*, 2005;

[1]School of Space Research, Kyung Hee University, Yongin-Si, Korea.
[2]Institute for Physical Science and Technology, University of Maryland, College Park, Maryland, USA.

Corresponding author: P. H. Yoon, Institute for Physical Science and Technology, University of Maryland, College Park, MD 20742, USA. (yoonp@umd.edu)

2169-9380/13/10.1002/2013JA019298

Burinskaya and Burch, 2007] or in nonuniform systems [*Le Quéau et al.*, 1985; *Cairns et al.*, 2011; *Pechhacker and Tsiklauri*, 2012]. A general nonlocal theory for the cyclotron maser instability is yet another unresolved problem.

[6] Moreover, recent efforts by a group of authors reconsider the cyclotron maser instability when there exist large-amplitude Alfvén waves [*Wu et al.*, 2012; *Zhao and Wu*, 2013]. According to these papers, the presence of intrinsic Alfvén waves not only leads to enhanced cyclotron maser excitation but also the underlying microscopic wave-particle interaction is fundamentally different than the customary cyclotron maser instability. In short, the problem of cyclotron maser is still an active research area with many outstanding issues.

[7] The purpose of the present paper is to revisit the classic loss cone-driven cyclotron maser instability problem and to discuss some detailed properties that have been overlooked in the past. Among the most important physical parameters that determine the instability excitation condition is the ratio of plasma-to-electron cyclotron frequencies, ω_p/Ω, where $\omega_p = (4\pi ne^2/m)^{1/2}$ and $\Omega = eB/mc$ are plasma and electron cyclotron frequencies, respectively, and n, e, m, c, and B being the ambient plasma density, unit electric charge, electron rest mass, speed of light in vacuo, and ambient magnetic field intensity, respectively. It is, therefore, instructive to consider how the growth rate varies as a function of ω_p/Ω.

[8] *Hewitt et al.* [1982] and *Melrose et al.* [1984] were among the first to investigate the properties of normalized maximum growth rate, $\gamma_{\max}/\Omega$, as a function of ω_p/Ω. Similar works were also carried out by *Sharma and Vlahos* [1984], *Winglee* [1985a, 1985b], *Winglee and Dulk* [1986], *Yoon et al.* [1996, 1998b, 2007], *Menietti et al.* [2010], *Wu et al.* [2012], *Zhao and Wu* [2013], and *Zhao et al.* [2013]. However, a common feature in all these works is that the focus was only on the maximum growth rate $\gamma_{\max}/\Omega$ as a function of ω_p/Ω. The detailed understanding of the maser emission also involves the dependence of the radiation emission angle and the frequency corresponding to the maximum growth, $\theta_{\max}$ and $(\omega_{\max} - s\Omega)/\Omega$, where $s = 1, 2, 3, \ldots$, on ω_p/Ω. The angular dependence may be important, for instance, in determining the radiation beaming pattern (see, e.g., *Calvert* [1987], who discusses observational aspects of the AKR beaming pattern). The present paper complements earlier works in that we provide a more complete picture on the maser instability by presenting results that show how $\gamma_{\max}/\Omega$, $\theta_{\max}$, and $(\omega_{\max} - s\Omega)/\Omega$ scale as functions of ω_p/Ω.

[9] The organization of the paper is as follows: In section 2, we outline the basic theoretical formalism and present some sample growth rate calculations. Section 3 is devoted to the discussion of the scaling behavior associated with the maximum growth rate, the emission angle, and the real frequency as a function of ω_p/Ω. Finally, the findings in the present paper are summarized in section 4.

2. Basic Theoretical Formalism and Sample Results

2.1. Magnetoionic Mode Dispersion Relation

[10] The wave dispersion relation is given by the magnetoionic mode theory, where the index of refraction for the extraordinary (X) and ordinary (O) mode branches are defined by

$$N_{\rm X}^2 = 1 - \frac{\omega_p^2}{\omega(\omega + \tau\Omega)},$$
$$N_{\rm O}^2 = 1 - \frac{\tau\omega_p^2}{\omega(\tau\omega - \Omega\cos^2\theta)}, \tag{1}$$

where $N = ck/\omega$ represents the index of refraction, k and ω being the wave number and angular frequency, respectively, θ is the angle of propagation for the wave phase velocity, and the quantity τ is given by

$$\tau = \left(\sigma + \sqrt{\sigma^2 + \cos^2\theta}\right)\frac{\omega_p^2 - \omega^2}{|\omega_p^2 - \omega^2|},$$
$$\sigma = \frac{\omega\Omega\sin^2\theta}{2|\omega^2 - \omega_p^2|}. \tag{2}$$

[11] The X and O modes are further classified into X and Z modes and O and W modes, depending on the frequency ranges. For $\omega > \omega_{\rm X}$, the X mode is called the "X" mode proper, where $\omega_{\rm X}$ is the X mode cutoff frequency,

$$\omega_{\rm X} = \frac{1}{2}\left(\sqrt{\Omega^2 + 4\omega_p^2} + \Omega\right). \tag{3}$$

This range is characterized by the superluminal condition, $\omega/k > c$. Superluminal modes are escaping radiations that can be detected by a remote observer, and we shall pay attention to such modes in the present paper. The other X mode branch called the "Z" mode is a trapped mode in the uniform plasma that cannot escape directly, and it is defined over a frequency range, $\omega_{\rm Z} < \omega < \omega_{\rm Z}^{\rm res}$. Here $\omega_{\rm Z}$ is the Z mode cutoff frequency,

$$\omega_{\rm Z} = \frac{1}{2}\left(\sqrt{\Omega^2 + 4\omega_p^2} - \Omega\right), \tag{4}$$

and $\omega_{\rm Z}^{\rm res}$ is the Z mode resonance frequency,

$$\omega_{\rm Z}^{\rm res} = \frac{1}{\sqrt{2}}\left[\omega_{\rm uh}^2 + \sqrt{(\omega_p^2 - \Omega^2)^2 + 4\omega_p^2\Omega^2\sin^2\theta}\right]^{1/2}, \tag{5}$$

where $\omega_{\rm uh}^2 = \omega_p^2 + \Omega^2$ is the upper hybrid frequency.

[12] The fast O mode ($\omega/k > c$) is defined over the range $\omega > \omega_p$ and is simply called the "O mode" proper. The slow mode ($\omega/k < c$) is defined in the low-frequency range, $\omega < \omega_{\rm W}^{\rm res}$, and is called the "W" mode. Here the resonance frequency $\omega_{\rm W}^{\rm res}$ is defined by

$$\omega_{\rm W}^{\rm res} = \frac{1}{\sqrt{2}}\left[\omega_{\rm uh}^2 - \sqrt{(\omega_p^2 - \Omega^2)^2 + 4\omega_p^2\Omega^2\sin^2\theta}\right]^{1/2}. \tag{6}$$

[13] The four magnetoionic modes, X, Z, O, and W, can be characterized by their polarization characteristics. Assuming that the ambient magnetic field lies along z axis, $\mathbf{B}_0 = B_0\hat{\mathbf{z}}$, and that the wave vector is in xz plane, $\mathbf{k} = \hat{\mathbf{x}}k\sin\theta + \hat{\mathbf{z}}k\cos\theta$, the unit electric field vector is given by

$$\mathbf{e} = \frac{\hat{\mathbf{x}}(K\sin\theta + T\cos\theta) + i\hat{\mathbf{y}} + \hat{\mathbf{z}}(K\cos\theta - T\sin\theta)}{(1 + K^2 + T^2)^{1/2}}, \tag{7}$$

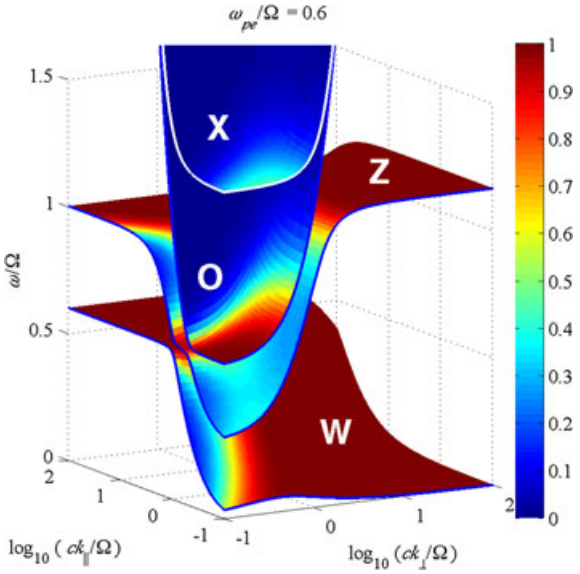

Figure 1. The magnetoionic dispersion surfaces: ω versus $k_\parallel = k\cos\theta$ and $k_\perp = k\sin\theta$, for $\omega_p/\Omega = 0.6$. The colormap indicates the degree of electrostatic polarization: Red means electrostatic, while blue indicates electromagnetic.

where K and T are two constants that characterize the mode polarization property,

$$K_{\rm X} = \frac{\omega_p^2}{\omega_p^2 - \omega^2}\frac{\Omega\sin\theta}{\omega + \tau\Omega},$$
$$K_{\rm O} = \frac{\omega_p^2}{\omega_p^2 - \omega^2}\frac{\tau\Omega\sin\theta}{\tau\omega - \Omega\cos^2\theta},$$
$$T_{\rm X} = \frac{\cos\theta}{\tau},$$
$$T_{\rm O} = -\frac{\tau}{\cos\theta}. \tag{8}$$

Here X means both X and Z, while O encompasses both O and W. The mode is purely longitudinal and electrostatic if $K = \infty$. The mode is purely transverse and electromagnetic if either $T = \infty$ or $T \neq 0$ and $K = 0$.

[14] The dispersion relation (1) may be plotted as dispersion surfaces, i.e., ω as a function of $k_\perp = k\sin\theta$ and $k_\parallel = k\cos\theta$. In Figure 1, we present a sample magnetoionic dispersion surfaces. The colormap represents the degree of longitudinal polarization,

$$\mathcal{L} \equiv \frac{K^2}{1 + K^2 + T^2}. \tag{9}$$

Dark red tones indicate that the mode is predominantly longitudinal, while blue indicates that the mode is transverse. As one can see, W and Z modes are largely electrostatic, except for quasi-parallel angles of propagation and for long wavelength regime. We shall not pay attention to these modes.

2.2. Temporal Growth/Damping Rate

[15] The general expression for fully relativistic temporal growth/damping rate for the magnetoionic mode is well known [e.g., *Melrose*, 1986b],

$$\Gamma = \frac{\pi}{2\omega}\frac{4\pi ne^2}{(1+T^2)R}\int d\mathbf{p}v_\perp^2 \sum_{s=-\infty}^{\infty} \times \left\{\frac{\gamma\omega}{\Omega}\left[K\sin\theta + T\left(\cos\theta - \frac{kv_\parallel}{\omega}\right)\right]\frac{J_s(b)}{b} + J_s'(b)\right\}^2 \times \delta\left(\omega - \frac{s\Omega}{\gamma} - k_\parallel v_\parallel\right)\left(\frac{s\Omega}{\gamma v_\perp}\frac{\partial}{\partial p_\perp} + k_\parallel\frac{\partial}{\partial p_\parallel}\right) f(p_\perp^2, p_\parallel). \tag{10}$$

Here $\gamma = (1 + p^2/m^2c^2)^{1/2}$ is the relativistic mass (Lorentz) factor, $\mathbf{p} = \gamma m\mathbf{v}$ defines the relation between the relativistic momentum and velocity, $\parallel$ and $\perp$ are defined with respect to the B field vector, $J_s(b)$ is the Bessel function, with the argument defined by $b = k_\perp v_\perp \gamma/\Omega$, and $f(p_\perp^2, p_\parallel)$ is the electron momentum distribution function. In the above, the mode designation associated with the quantities K, T, and R is omitted. Of these, K and T are already introduced, but R is another magnetoionic parameter related to the group velocity,

$$R_{\rm X} = 1 + \frac{\omega_p^2(\tau^2\omega^2 - \omega_p^2\cos^2\theta)}{\omega^2(\omega + \tau\Omega)^2\sin^2\theta}\frac{\tau^2 - \cos^2\theta}{\tau^2 + \cos^2\theta},$$
$$R_{\rm O} = 1 + \frac{\omega_p^2\cot^2\theta(\tau^2\omega^2 - \omega_p^2\cos^2\theta)}{\omega^2(\tau\omega - \Omega\cos^2\theta)^2}\frac{\tau^2 - \cos^2\theta}{\tau^2 + \cos^2\theta}. \tag{11}$$

[16] In what follows, we make use of the weakly relativistic approximation in which we replace the relativistic mass factor by unity everywhere, except in the resonance condition, where it is replaced by $\gamma \approx 1 + p^2/(2m^2c^2)$. Upon carrying out one component of the vector momentum integral by virtue of the delta function resonance condition, it is possible to show that the temporal growth rate reduces to

$$\Gamma = \frac{\omega_p^2}{\omega}\frac{\pi^2}{R}\sum_{s=0}^{\infty}\left(\Theta(s\Omega - \omega)\int_{-1}^{1} d\mu Q_s(u_+, \mu) + \Theta(\omega - s\Omega)\Theta(1 - \mu_s^2)\int_{\mu_s}^{1} d\mu \sum_{+,-} Q_s(u_\pm, \mu)\right),$$
$$u_\pm = N\mu\cos\theta \pm \sqrt{N^2\mu^2\cos^2\theta + 2\left(\frac{s\Omega}{\omega} - 1\right)},$$
$$\mu_s = \frac{\sqrt{2}}{N\cos\theta}\sqrt{1 - \frac{s\Omega}{\omega}}, \tag{12}$$

where the integrand $Q(u, \mu)$ is defined for each X and O modes as follows:

$$Q_s^{\rm X}(u,\mu) = \frac{\tau^2}{\tau^2 + \cos^2\theta}\frac{u^2(1-\mu^2)}{|u - N_{\rm X}\mu\cos\theta|} \times \left[\frac{\omega}{\Omega}\left(K_{\rm X}\sin\theta + \frac{\cos\theta}{\tau}(\cos\theta - N_{\rm X}u\mu)\right)\frac{J_s(b)}{b} + J_s'(b)\right]^2 \times \left(u\frac{\partial}{\partial u} + (N_{\rm X}u\cos\theta - \mu)\frac{\partial}{\partial\mu}\right) f(u,\mu),$$

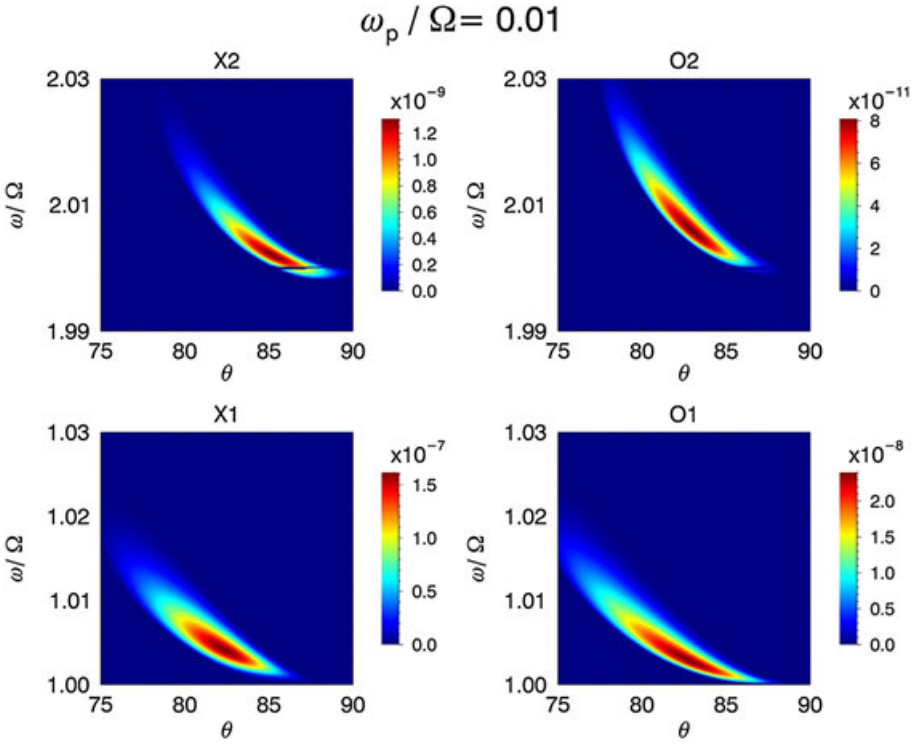

Figure 2. The growth rates for (left) the first and second harmonic X modes and (right) the two harmonic O modes versus ω/Ω and θ, for $\omega_p/\Omega = 0.01$.

$$Q_s^{\mathrm{O}}(u,\mu) = \frac{1}{\tau^2+\cos^2\theta}\frac{u^2(1-\mu^2)}{|u-N_{\mathrm{O}}\mu\cos\theta|} \times\left[\frac{\omega}{\Omega}\left(K_{\mathrm{O}}\sin\theta\cos\theta-\tau(\cos\theta-N_{\mathrm{O}}u\mu)\right) \times\frac{J_s(b)}{b}+J_s'(b)\right]^2 \times\left(u\frac{\partial}{\partial u}+(N_{\mathrm{O}}u\cos\theta-\mu)\frac{\partial}{\partial\mu}\right)f(u,\mu), \quad (13)$$

where $u = p/mc$ is the normalized momentum, $\mu = p_\parallel/p$ represents the cosine of the pitch angle, and $b = (\omega/\Omega)Nu(1-\mu^2)^{1/2}\sin\theta$ is the argument of the Bessel function.

[17] For the choice of distribution function $f(u,\mu)$, we choose one-sided loss cone model. Such a model is well supported by satellite observation in the AKR source region [*Ergun et al.*, 2000] and the source region of the Saturn kilometric radiation [*Schippers et al.*, 2011]. The recent analysis by *Mutel et al.* [2007] also employed such a model electron distribution. The mathematical form of the loss cone distribution adopted in the present paper can be constructed on the basis of adiabatic constants $\mathcal{M} = v_\perp^2/B$ and $H = (m^2/2)(v_\perp^2+v_\parallel^2)$, where magnetic field intensity B is a function of distance along the field line. In this case, the electron distribution function is given by an arbitrary function of $\mathcal{M}$ and H. Since $\mathcal{M}$ and H are constants along the field, we generally have the following relations among the velocity variables at any two locations z and z' along the field:

$$v_\perp^2(z) = \frac{B(z)}{B(z')}v_\perp^2(z'),$$

$$v_\parallel^2(z) = v_\parallel^2(z') + v_\perp^2(z')\left(1-\frac{B(z)}{B(z')}\right).$$

If we assume that B is given by a dipole model, $B(z) \propto (R_E+z)^{-3}$, where $R_E = 6371$ km is the Earth radius, and if we assume a suitable ionospheric (loss cone) boundary, z_M, below which the auroral electrons precipitate to the Earth's upper atmosphere and be lost, then the condition for precipitating electrons are $v_\parallel^2(z_M) > 0$, while the reflected electrons satisfy the opposite equality, $v_\parallel^2(z_M) < 0$. If we express the cosine of the pitch angle by $\mu = v_\parallel/v$, then the conditions for precipitating or reflecting electrons leads to the definition of the loss cone pitch angle boundary

$$\mu_0^2 = \frac{B(z_M)-B(z)}{B(z_M)}.$$

As an example, we may choose $z_M = 100$ km, which can be considered as the bottom of the ionosphere. In the present context, however, the details of the ionospheric model is unimportant since we shall simply specify the value of μ_0.

[18] If the loss cone boundary is perfectly sharp, then the loss cone distribution may be constructed as

$$f(u,\mu) \propto \exp\left(-\frac{u^2}{\alpha^2}\right)\Theta(\mu-\mu_0),$$

where we now switch to normalized momentum variable, $u = p/mc$, and $\Theta(x)$ is the Heaviside step function, and $\Theta(x) = 1$ for $x > 0$ and zero otherwise. However, an infinitely sharp loss cone model is not only incompatible with kinetic growth rate analysis but also unphysical since a number of microscopic plasma processes can easily lead to the erosion of the loss cone boundary. We thus replace $\Theta(\mu-\mu_0)$ by a smoothed factor $(1/2)\{1-\tanh[(\mu-\mu_0)/\delta]\}$, where δ is an arbitrary parameter that determines the smoothness

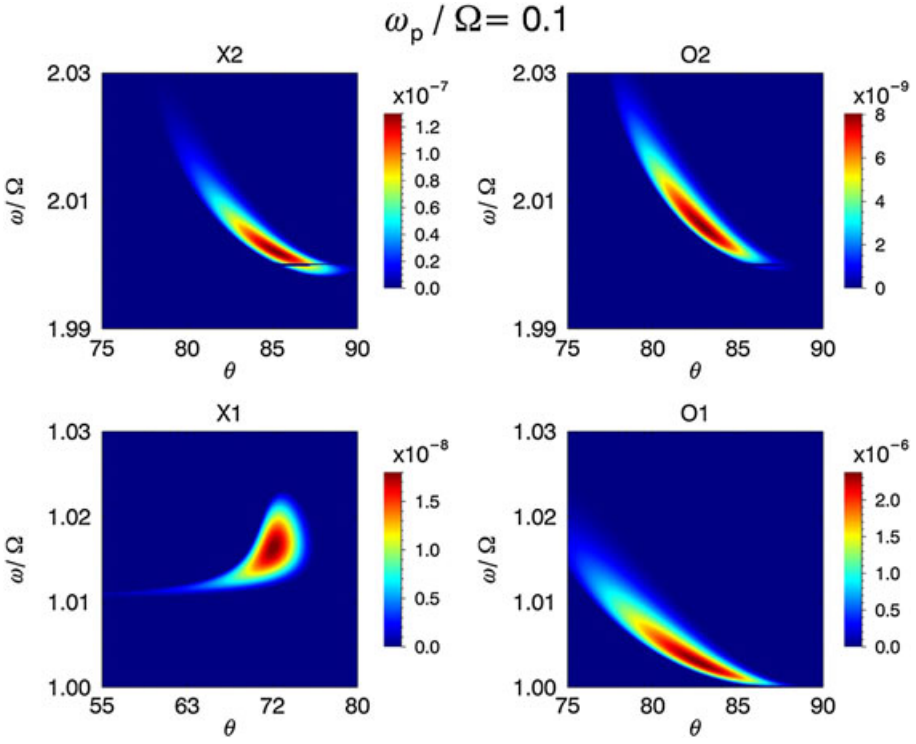

Figure 3. The same as Figure 2, except that $\omega_p/\Omega = 0.1$. For X1 mode, vertical axis (i.e., frequency range) below 1.01 is unphysical since the cutoff frequency for X mode is at $\omega_X/\Omega = 1.01$.

associated with the loss cone pitch angle boundary. We thus model the loss cone electron distribution by

$$f(u,\mu) = \frac{1}{\pi^{3/2}\alpha^3 A}\exp\left(-\frac{u^2}{\alpha^2}\right)\left(1-\tanh\frac{\mu-\mu_0}{\delta}\right),$$
$$A = 1+\frac{\delta}{2}\left[\ln\left(\cosh\frac{1+\mu_0}{\delta}\right)-\ln\left(\cosh\frac{1-\mu_0}{\delta}\right)\right], \quad (14)$$

where $\alpha = (2T_e/mc^2)^{1/2}$ represents the normalized thermal speed, T_e being the electron temperature defined in the unit of energy, μ_0 is the cosine of the loss cone angle, and δ is a parameter that defines the smoothness associated with the loss cone boundary. In addition to the energetic loss cone electrons, we also consider the background thermal electrons. In the stability analysis to follow, we consider that the ratio of number densities for the energetic-to-background electrons is 10%. The temperature for the cold electrons is assumed to be $\sim 10^3$ K, corresponding to the normalized thermal speed $\alpha_0 = (2T_0/mc^2)^{1/2} = 5.8\times10^{-4}$.

2.3. Sample Growth/Damping Rates

[19] In what follows, we consider a sample case of $\alpha = 0.1$ (corresponding to 2.56 keV thermal electron energy), $\mu_0 = 0.6$ (implying that the pitch angle corresponding to the loss cone is equal to 53.13°), the smoothness parameter $\delta = 0.25$, and a range of plasma-to-gyro frequency ratio, ω_p/Ω. Figure 2 shows the growth rates for first and second harmonic X modes (designated by X1 and X2) and the two harmonic O modes (O1 and O2), plotted as a function of ω/Ω and θ, for $\omega_p/\Omega = 0.01$. In this case, the most robust exponential wave growth occurs for fundamental X mode (X1). It is well known that for low-density plasmas, the most important cyclotron maser mode is the fundamental X mode, and the Earth AKR is a prime example. In the case of AKR, the large-scale parallel electric field removes the cold electrons during disturbed geomagnetic periods, thus temporarily lowering the plasma density along the auroral field lines. Note that all the wave excitation occurs in oblique directions, $\theta \approx 80°$ or so, and the wave frequency for each harmonic is close to the integer value that defines the cyclotron harmonic.

[20] In Figure 3, we plot the growth rate in the same format as Figure 2 and for the same set of input parameters, except that the frequency ratio is increased to $\omega_p/\Omega = 0.1$. In this case, the most important mode (i.e., with the highest temporal growth rate) is the fundamental O mode (O1).

[21] Moving on to the case of relatively high plasma density, $\omega_p/\Omega = 1$, the growth rate plots in Figure 4 show that there is no X1 mode. This is because the cutoff frequency for X mode is substantially higher than the fundamental electron cyclotron frequency. X1 mode can be excited only if the X1 mode cutoff frequency is sufficiently close to the fundamental electron cyclotron frequency, which can happen only if ω_p/Ω is sufficiently small. In this case, the growth rates for X2 and O2 modes are comparable.

[22] The basic mechanism for the maser instability is the relativistic cyclotron resonance between the electrons and waves. In the weakly relativistic approximation, the resonance condition $\omega - s\Omega/\gamma - k_\parallel v_\parallel = 0$ can be expressed as

$$u_\perp^2 + (u_\parallel - u_0)^2 = r^2,$$
$$u_0 = N\cos\theta,$$
$$r^2 = N^2\cos^2\theta + \frac{2(s\Omega-\omega)}{\omega}. \quad (15)$$

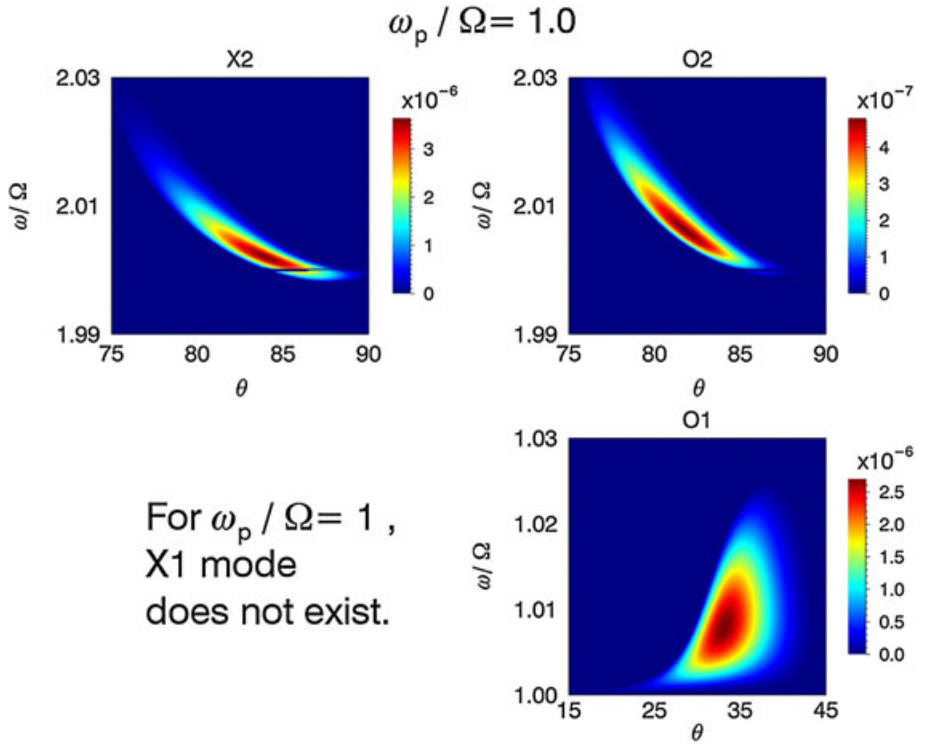

Figure 4. The same as the previous two figures, except that $\omega_p/\Omega = 1$. In this case, however, there is no X1 mode maser instability since X mode cutoff frequency is higher than the fundamental cyclotron frequency.

If we consider the case of $\omega_p/\Omega = 0.1$, we find that the most unstable mode, i.e., O1, is characterized by the frequency and propagation angle $(\omega, \theta) \sim (1.10017\Omega, 82.5°)$ at which the highest growth occurs. In comparison, the local maximum for the X1 mode growth rate occurs at $(\omega, \theta) \sim (1.1014\Omega, 72°)$. Making use of these inputs, we may compute the resonance circles corresponding to X1 and O1 modes, given by equation (15), in the case of $\omega_p/\Omega = 0.1$, and superpose the results on the contour plot of the model loss cone distribution function. The result is shown Figure 5.

3. Instability Analysis Near Maximum Growth Conditions

[23] The case studies in the previous section show that the cyclotron maser excitation occurs at individual harmonics of the electron gyrofrequency, but the actual growth rates for each mode varies depending on the frequency ratio ω_p/Ω. As noted in section 1, this dependence has been noted by many researchers, and efforts have been made to investigate how the (local) maximum growth rate for each harmonic X and O modes scale as ω_p/Ω is either increased or decreased. However, in all the earlier works, focus has been paid exclusively to the maximum growth rate γ_{max}/Ω, even though this is only one of the physical quantities that characterize the maser instability. The other two quantities are the wave propagation angle corresponding to the (local) maximum growths, θ_{max}, and the frequency at which the maximum growth occurs. Since each harmonic mode grows in the vicinity of the cyclotron harmonics, the relevant quantity, as far as the frequency is concerned, maybe the frequency at each harmonic with the harmonic mode number subtracted, $(\omega_{max} - s\Omega)/\Omega$.

[24] Figure 6 plots the local maximum growth rate γ_{max}/Ω for each harmonic X and O modes as a function of ω_p/Ω

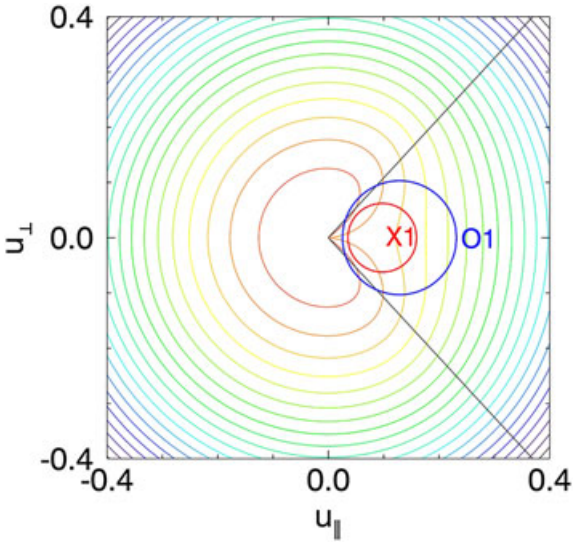

Figure 5. Contour plot of the logarithmic of the distribution function $f(u, \mu)$ versus $u_\perp$ and $u_\parallel$, for $\alpha = 0.1$, $\mu_0 = 0.6$, and $\delta = 0.25$. The cold background component is not included in the contour plot. Superposed are two resonance circles for X1 and O1 modes in the case of $\omega_p/\Omega = 0.1$. The frequencies and angles for these modes are chosen according to their local maximum growth conditions.

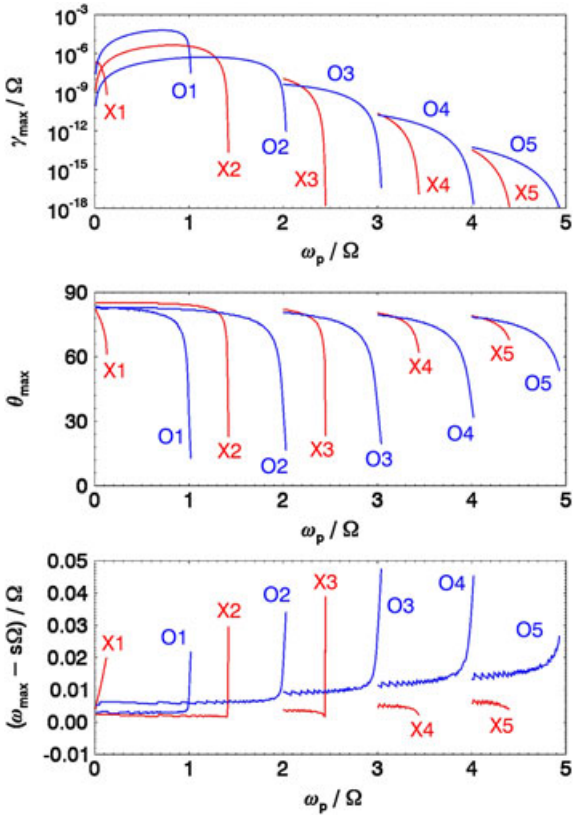

Figure 6. The γ_{max}/Ω, θ_{max}, and $(\omega_{max}-s\Omega)/\Omega$ versus ω_p/Ω, for $\alpha = 0.1$ (2.56 keV electron thermal energy) and $\mu_0 = 0.6$ (or 53.13° loss cone angle).

(top), for $\alpha = 0.1$ (corresponding to 2.56 keV electron thermal energy) and $\mu_0 = 0.6$ (or 53.13° loss cone angle). Similar plots such as this can be found in the literature in one form or another, as outlined in section 1. However, the behavior of θ_{max} and $(\omega_{max} - s\Omega)/\Omega$ has not been systematically investigated before. In Figure 6 (middle), we display how the maximum angle, θ_{max}, scales as ω_p/Ω is varied. This information may be crucial for determining the radiation emission pattern. Finally, in the third panel, we plot the maximum frequency $(\omega_{max} - s\Omega)/\Omega$, where $s = 1, 2, 3, 4, 5$, depending on the mode designations, X1, X2, …, O1, O2 etc., in that order. As one can see, as ω_p/Ω increases, the maser mode excitation moves to higher harmonics. For increasing ω_p/Ω, the propagation angle for all the modes first start from quasi-perpendicular directions but systematically to quasi-parallel direction before the maser modes at a given harmonic are stabilized, and the next harmonic modes are excited. This pattern repeats for all the harmonics that we have investigated, up to fifth harmonics. The frequencies for each harmonic modes start very close to the integer harmonic mode number but systematically deviate away from the harmonic value before the instability switches to the next harmonic.

[25] Next, we increase the thermal speed to $\alpha = 1/\sqrt{10} \approx 0.3126$, and the result is shown in Figure 7, in the same format as Figure 6. For the present case of slightly hotter loss cone electrons, we find that the X1 mode maser is operative over a wider range of ω_p/Ω, until it eventually becomes stable. In general, the decrease in γ_{max} and θ_{max} at each harmonic for increasing ω_p/Ω is more gradual when compared with the case of $\alpha = 0.1$. Note that the range of frequency deviation is also an order of magnitude wider than the previous case.

[26] Figure 8 is the same as Figures 6 or 7 except that we now increase the thermal speed to $\alpha = 1$. In this case, we found that X1 mode is stabilized for all ω_p/Ω. For low values of ω_p/Ω, even O1 mode is also stable, but for $0.5 \leq \omega_p/\Omega \leq 1$ or so, the fundamental O mode manages to have a finite growth rate. The overall behavior associated with γ_{max}/Ω, θ_{max}, and $(\omega_{max} - s\Omega)/\Omega$ versus ω_p/Ω is qualitatively similar to the previous two cases of $\alpha = 0.1$ and $\alpha = 1/\sqrt{10}$, but there are quantitative differences, as Figure 8 illustrates. In particular, the spread in the frequency variation is much wider than the two previous cases.

[27] Now, we should note that the model distribution function (14) is in the form of nonrelativistic Maxwellian distribution (with the loss cone pitch angle anisotropy factor multiplied). On the other hand, the thermal speed of $\alpha = 1$ corresponds to relativistic temperature. Physically, this means that the bulk of the electrons in the Maxwellian model have superluminal speeds, which is of course unphysical. Consequently, the above discussion associated with Figure 8 should be taken with this limitation in mind. One could correct this problem by replacing the model distribution with the relativistic Jüttner type of model, $e^{-(mc^2/T)\sqrt{1+p^2/m^2c^2}}$ and making use of the fully relativistic Lorentz factor in the cyclotron resonance condition. However, such a task, although not too difficult, is beyond the scope of the present paper.

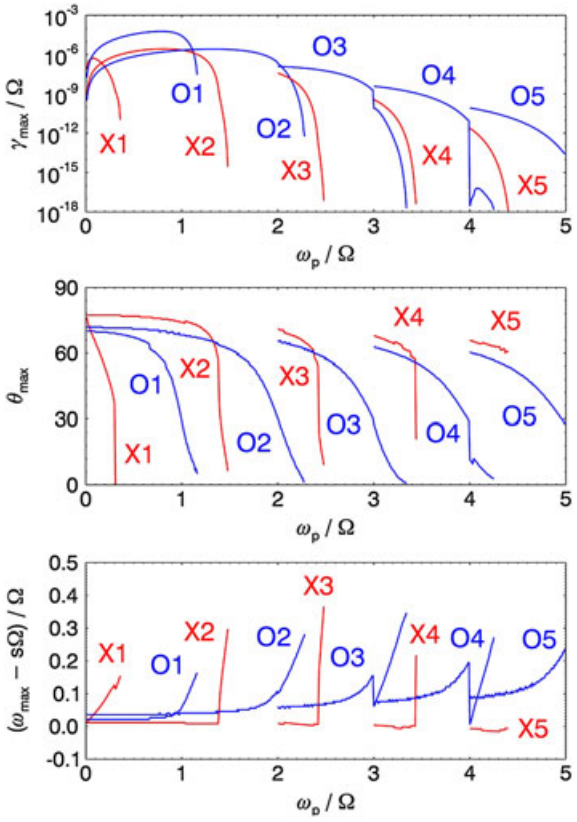

Figure 7. The γ_{max}/Ω, θ_{max}, and $(\omega_{max} - s\Omega)/\Omega$ versus ω_p/Ω, for $\alpha = 1/\sqrt{10} \approx 0.3126$ and $\mu_0 = 0.6$.

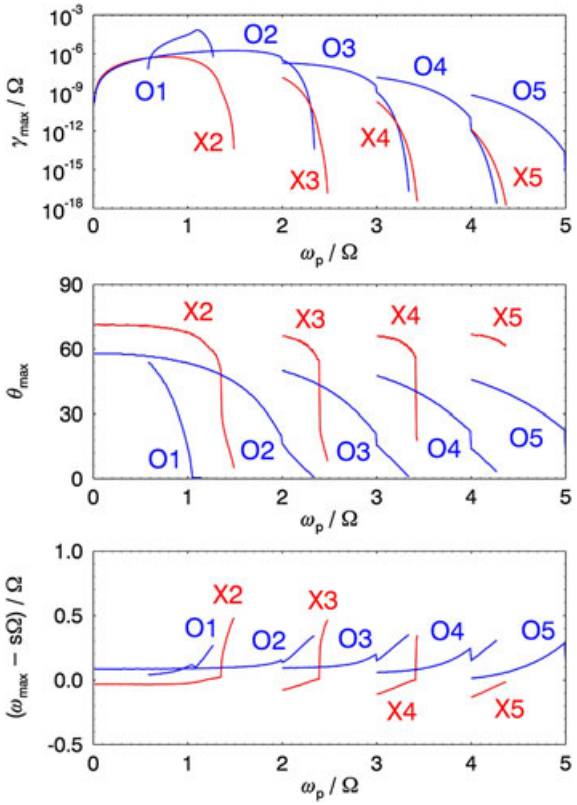

Figure 8. The γ_{max}/Ω, θ_{max}, and $(\omega_{max} - s\Omega)/\Omega$ versus ω_p/Ω, for $\alpha = 1$ and $\mu_0 = 0.6$.

[28] We also varied the loss cone angle (and the corresponding $\mu_0 = \cos\theta_0$, where θ_0 is the loss cone angle), from 53.13° (or $\mu_0 = 0.6$) in the case of Figure 6 to 30° and to 60°, but the results showed that the maser instability characteristics do not depend too critically on the variation of the loss cone angle. The only differences were that the wider loss cone angle produced higher growth rate, but otherwise, the overall scaling characteristics of γ_{max}, θ_{max}, and ω_{max} as functions of ω_p/Ω were qualitatively similar. Consequently, we do not display the results.

4. Summary

[29] The present paper revisited the weakly (or mildly) relativistic cyclotron maser instability driven by loss cone electron distribution function. Despite the fact that the details of the maser instability are well known in the literature, largely owing to researches devoted to the study of the Earth's auroral kilometric radiation (AKR), which took place in the 1980s and 1990s, most available theoretical investigations of the gross instability properties emphasize how the normalized local maximum growth rate, γ_{max}/Ω, varies as a function of ω_p/Ω. In order to complete the analysis, we analyzed additional properties, namely the radiation emission angle corresponding to the maximum growth, θ_{max}, as well as the frequency corresponding to the maximum growth rate at each harmonic, $(\omega_{max} - s\Omega)/\Omega$, where $s = 1, 2, 3, \ldots$, as a function of ω_p/Ω.

[30] We found that in accordance with the known results in the literature, low-density (or strongly magnetized) plasmas characterized by low ω_p/Ω support the excitation of low-harmonic X and O modes, but as ω_p/Ω increases, the harmonic mode number corresponding to the maser instability excitation shifts upward accordingly. New findings associated with the scaling behavior of θ_{max} and the harmonic-adjusted frequency $(\omega_{max} - s\Omega)/\Omega$ are that first, the excitation of harmonic X and O modes takes place very close to the 90° propagation angle as ω_p/Ω is increased. However, as ω_p/Ω further increases (and the maximum growth rate decreases), the emission angle turns more and more field aligned, until the harmonic modes cease to grow, and the next higher harmonic modes begin to get excited. Similarly, the harmonic-adjusted frequency stays very close to zero value when the maser modes for each harmonic are excited, but as ω_p/Ω increases, the frequencies begin to deviate from the given harmonic, until they increase or decrease, sometimes rather sharply, before the maser mode at the given harmonic is suppressed, and the next harmonic maser mode gets excited. These patterns repeat themselves for each higher harmonic.

[31] We also found that among the physical input parameters that determine the maser instability, the thermal energy associated with the loss cone electrons have the most significant impact on the scaling properties of the above-mentioned quantities. Changing the loss cone angle only produced the quantitative differences, which we did not show. Obviously, the ratio of number densities associated with the loss cone electrons versus the background electrons must also affect the maser growth rate, but since the growth is linearly proportional to this ratio, we did not systematically vary this parameter.

[32] In summary, by revisiting the classical weakly relativistic electron-cyclotron maser instability driven by loss cone distribution and investigating the detailed properties associated with the two fast magnetoionic modes, we have unveiled some interesting scaling behavior inherent in the cyclotron maser instability growth, propagation, and spectral properties.

[33] **Acknowledgments.** This research was supported by WCU grant R31-10016 from the Korean Ministry of Education, Science and Technology and the BK21 plus program through the National Research Foundation (NRF) funded by the Ministry of Education of Korea to the Kyung Hee University, Korea, and by NSF grant AGS1147759 to the University of Maryland.

[34] Philippa Browning thanks the reviewer for assistance in evaluating this paper.

References

Begelman, M. C., R. E. Ergun, and M. J. Rees (2005), Cyclotron maser emission from blazar jets?, *Astrophys. J.*, *625*, 51.

Benson, R. F., W. Calvert, and D. M. Klumpar (1980), Simultaneous wave and particle observations in the auroral kilometric radiation source region, *Geophys. Res. Lett*, *7*, 959.

Bingham, R., B. J. Kellett, R. A. Cairns, J. Tonge, and J. T. Mendonça (2003), Cyclotron maser radiation from astrophysical shocks, *Astrophys. J*, *595*, 279.

Bingham, R., B. J. Kellett, R. A. Cairns, A. D. R. Phelps, K. Ronald, and D. Speirs (2004), Cyclotron maser radiation in space and laboratory plasmas, *Contrib. Plasma Phys.*, *44*, 382.

Burinskaya, T. M., and J. L. Burch (2007), Waveguide regime of cyclotron maser instability plasma regions of depressed density, *Plasma Phys. Rep.*, *33*, 28.

Cairns, R. A., et al. (2011), Cyclotron maser radiation from an inhomogeneous plasma, *Phys. Plasmas*, *18*, 022,902, doi:10.1063/1.3551697.

Calvert, W. (1982), A feedback model for the source of auroral kilometric radiation, *J. Geophys. Res*, *87*, 8199.

Calvert, W. (1987), Hollowness of the observed auroral kilometric radiation pattern, *J. Geophys. Res*, *92*, 1267.

Ergun, R. E., C. W. Carlson, J. P. McFadden, and G. T. Delory (2000), Electron-cyclotron maser driven by charged-particle acceleration from magnetic field-aligned electric fields, *Astrophys. J*, *538*, 456.

Farrell, W. M., M. D. Desch, and P. Zarka (1999), On the possibility of coherent cyclotron emission from extrasolar planets, *J. Geophys. Res*, *104*, 14,025.

Gurnett, D. A. (1974), The Earth as a radio source: Terrestrial kilometric radiation, *J. Geophys. Res*, *79*, 4227.

Gurnett, D. A., R. R. Anderson, F. L. Scarf, R. W. Fredericks, and E. J. Smith (1979), Initial results from the ISEE-1 and -2 plasma wave investigation, *Space Sci. Rev.*, *23*, 103.

Gurnett, D. A., et al. (2004), The Cassini radio and plasma wave investigation, *Space Sci. Rev.*, *114*, 395–463.

Hallinan, G., et al. (2007), Periodic bursts of coherent radio emission from an ultracool dwarf, *Astrophys. J.*, *663*, L25–L28.

Hallinan, G., A. Antonova, J. G. Doyle, S. Bourke, C. Lane, and A. Golden (2008), Confirmation of the electron cyclotron maser instability as the dominant source of radio emission from very low mass stars and brown dwarfs, *Astrophys. J*, *684*, 644.

Hess, S., F. Mottez, and P. Zarka (2007), Jovian *S* burst generation by Alfvén waves, *J. Geophys. Res*, *112*, A11212, doi:10.1029/2006JA012191.

Hewitt, R. G., D. B. Melrose, and K. G. Rönnmark (1982), The loss-cone driven electron-cyclotron maser, *Aust. J. Phys.*, *35*, 447.

Lee, L. C., and C. S. Wu (1980), Amplification of radiation near cyclotron frequency due to electron population inversion, *Phys. Fluids*, *23*, 1348.

Lee, K. H., Y. Omura, L. C. Lee, and C. S. Wu (2009), Nonlinear saturation of cyclotron maser instability associated with energetic ring-beam electrons, *Phys. Rev. Lett.*, *103*, 105,101, doi:10.1103/PhysRevLett.103.105101.

Le Quéau, D., R. Pellat, and A. Roux (1985), The maser synchrotron instability in an inhomogeneous medium: Application to the generation of the auroral kilometric radiation, *Ann. Geophys.*, *3*, 273.

Louran, P., A. Roux, H. de Fédraudy, and D. Le Qu'eau (1990), Trapped electrons as a free energy source for the auroral kilometric radiation, *J. Geophys. Res.*, *95*, 5983.

Louarn, P., and D. Le Qu'eau (1996), Generation of the auroral kilometric radiation in plasma cavities - II. The cyclotron maser instability in small size sources, *Planet. Space Sci.*, *44*, 211.

Melrose, D. B., R. G. Hewitt, and G. A. Dulk (1984), Electron-cyclotron maser emission: Relative growth and damping rates for different modes and harmonics, *J. Geophys. Res*, *89*, 897.

Melrose, D. B. (1986a), A phase-bunching mechanism for fine structures in auroral kilometric radiation and Jovian decametric radiation, *J. Geophys. Res.*, *91*, 7970.

Melrose, D. B. (1986b), *Instabilities in Space and Laboratory Plasmas*, Cambridge Univ. Press, Cambridge.

Menietti, J. D., P. H. Yoon, S.-Y. Ye, B. Cecconi, and A. M. Rymer (2010), Source mechanism of Saturn narrowband emission, *Ann. Geophys.*, *28*, 1013.

Mutel, R. L., W. M. Peterson, T. R. Jaeger, and J. D. Scudder (2007), Dependence of cyclotron maser instability growth rates on electron velocity distributions and perturbation by solitary waves, *J. Geophys. Res.*, *112*, A07211, doi:10.1029/2007JA012442.

Nichols, J. D., M. R. Burleigh, S. L. Casewell, S. W. H. Cowley, G. A. Wynn, J. T. Clarke, and A. A. West (2012), Origin of electron cyclotron maser induced radio emissions at ultracool dwarfs: Magnetosphere-ionosphere coupling currents, *Astrophys. J.*, *760*, 59.

Pechhacker, R., and D. Tsiklauri (2012), Electron cyclotron maser emission mode coupling to the *z*-mode on a longitudinal density gradient in the context of solar type III bursts, *Phys. Plasmas*, *19*, 110702, doi:10.1063/1.4769104.

Pottelette, R., R. A. Treumann, M. Berthomier, and J. Jasperse (2003), Electrostatic shock properties inferred from AKR fine structure, *Nonlinear Processes Geophys.*, *10*, 87.

Pritchett, P. L. (1984), Relativistic dispersion, the cyclotron maser instability, and auroral kilometric radiation, *J. Geophys. Res*, *89*, 8957.

Pritchett, P. L., and R. J. Strangeway (1985), A simulation study of kilometric radiation generation along an auroral field line, *J. Geophys. Res*, *90*, 9650.

Pritchett, P. L. (1986), Cyclotron maser radiation from a source structure localized perpendicular to the ambient magnetic field, *J. Geophys. Res*, *91*, 13,569.

Pritchett, P. L., and R. M. Winglee (1989), Generation and propagation of kilometric radiation in the auroral plasma cavity, *J. Geophys. Res*, *94*, 129.

Pritchett, P. L., R. J. Strangeway, C. W. Carlson, R. E. Ergun, J. P. McFadden, and G. T. Delory (1999), Free energy sources and frequency bandwidth for the auroral kilometric radiation, *J. Geophys. Res*, *104*, 10,317.

Schippers, P., et al. (2011), Auroral electron distributions within and close to the Saturn kilometric radiation source region, *J. Geophys. Res.*, *116*, A05203, doi:10.1029/2011JA016461.

Sharma, R. R., and L. Vlahos (1984), Comparative study of the loss cone-driven instabilities in the low solar corona, *Astrophys. J.*, *280*, 405.

Speirs, D. C., et al. (2010), Numerical investigation of auroral cyclotron maser processes, *Phys. Plasmas*, *17*, 056,501, doi:10.1063/1.3371937.

Tang, J. F., and D. J. Wu (2009), Electron-cyclotron maser emission by power-law electrons in coronal loops, *Astron. Astrophys.*, *493*, 623.

Treumann, R. A. (2006), The electron-cyclotron maser for astrophysical application, *Astron. Astrophys. Rev.*, *13*, 229, doi:10.1007/s00159-006-0001-y.

Treumann, R. A., W. Baumjohann, and R. Pottelette (2011), Electron-cyclotron maser radiation from electron holes: Upward current region, *Ann. Geophys.*, *29*, 1885, doi:10.5194/angeo-29-1885-2011.

Trigilio, C., P. Leto, G. Umana, C. S. Buemi, and F. Leone (2011), Auroral radio emission from stars: The case of CU Virginis, *Astrophys. J.*, *739*, L10.

Vorgul, I., R. A. Cairns, and R. Bingham (2005), Analysis of a cyclotron maser instability in cylindrical geometry, *Phys. Plasmas*, *12*, 122,903.

Willes, A. J., and K. Wu (2004), Electron-cyclotron maser emission from white dwarf pairs and white dwarf planetary systems, *Mon. Not. R. Astron. Soc.*, *348*, 285.

Winglee, R. M. (1985a), Effects of a finite plasma temperature on electron-cyclotron maser emission, *Astrophys. J.*, *291*, 160.

Winglee, R. M. (1985b), Fundamental and harmonic electron cyclotron maser emission, *J. Geophys. Res*, *90*, 9663.

Winglee, R. M., and G. A. Dulk (1986), The electron-cyclotron maser instability as a source of plasma radiation, *Astrophys. J.*, *307*, 808.

Winglee, R. M., and P. L. Pritchett (1986), The generation of low-frequency electrostatic waves in association with auroral kilometric radiation, *J. Geophys. Res.*, *91*, 13,531.

Wu, C. S., and L. C. Lee (1979), A theory of the terrestrial kilometric radiation, *Astrophys. J.*, *230*, 621.

Wu, C. S., C. B. Wang, D. J. Wu, and K. H. Lee (2012), Resonant wave-particle interactions modified by intrinsic Alfvénic turbulence, *Phys. Plasmas*, *19*, 082,902, doi:10.1063/1.4742989.

Yoon, P. H., A. T. Weatherwax, and T. J. Rosenberg (1996), Lower ionospheric cyclotron maser theory: A possible source of $2f_{ce}$ and $3f_{ce}$ auroral radio emissions, *J. Geophys. Res.*, *101*, 27,015.

Yoon, P. H., and A. T. Weatherwax (1998a), A theory for AKR fine frequency structure, *Geophys. Res. Lett.*, *25*, 4461.

Yoon, P. H., A. T. Weatherwax, and T. J. Rosenberg (1998b), On the generation of auroral radio emissions at harmonics of the lower ionospheric electron cyclotron frequency: *X*, *O*, and *Z* mode maser calculations, *J. Geophys. Res.*, *103*, 4071.

Yoon, P. H., C. B. Wang, and C. S. Wu (2007), Ring-beam driven maser instability for quasi-perpendicular shocks, *Phys. Plasmas*, *14*, 022,901, doi:10.1063/1.2437118.

Zarka, P. (1998), Auroral radio emissions at the outer planets: Observations and theories, *J. Geophys. Res.*, *103*, 20,159.

Zhao, G. Q., and C. S. Wu (2013), Emission of radiation induced by pervading Alfvén waves, *Phys. Plasmas*, *20*, 034,503, doi:10.1063/1.4798493.

Zhao, G. Q., L. Chen, Y. H. Yan, and D. J. Wu (2013), Effects of Alfvén waves on electron cyclotron maser emission in coronal loops and solar type I radio storms, *Astrophys. J.*, *770*, 75.